Journal of Advanced Ceramics
2023, **12**(5): 1090–1104
https://doi.org/10.26599/JAC.2023.9220741
ISSN 2226-4108
CN 10-1154/TQ

Research Article

Influence of average radii of RE^{3+} ions on phase structures and thermal expansion coefficients of high-entropy pyrosilicates

Zeyu Chen[a,b], Chucheng Lin[a], Wei Zheng[a], Xuemei Song[a,b], Caifen Jiang[a], Yaran Niu[c], Yi Zeng[a,*]

[a]*State Key Lab of High Performance Ceramics and Superfine Microstructure, Shanghai Institute of Ceramics, Chinese Academy of Sciences, Shanghai 200050, China*
[b]*Center of Materials Science and Optoelectronics Engineering, University of Chinese Academy of Sciences, Beijing 100049, China*
[c]*Key Laboratory of Inorganic Coating Materials CAS, Shanghai Institute of Ceramics, Chinese Academy of Sciences, Shanghai 200050, China*

Received: November 6, 2022; Revised: February 6, 2023; Accepted: March 5, 2023

Abstract: High-entropy pyrosilicate element selection is relatively blind, and the thermal expansion coefficient (CTE) of traditional β-type pyrosilicate is not adjustable, making it difficult to meet the requirements of various types of ceramic matrix composites (CMCs). The following study aimed to develop a universal rule for high-entropy pyrosilicate element selection and to achieve directional control of the thermal expansion coefficient of high-entropy pyrosilicate. The current study investigates a high-entropy design method for obtaining pyrosilicates with stable β-phase and γ-phase by introducing various rare-earth (RE) cations. The solid-phase method was used to create 12 different types of high-entropy pyrosilicates with 4–6 components. The high-entropy pyrosilicates gradually transformed from β-phase to γ-phase with an increase in the average radius of RE^{3+} ions ($\bar{r}(RE^{3+})$). The nine pyrosilicates with a small $\bar{r}(RE^{3+})$ preserve β-phase or γ-phase stability at room temperature to the maximum of 1400 ℃. The intrinsic relationship between the thermal expansion coefficient, phase structure, and RE–O bond length has also been found. This study provides the theoretical background for designing high-entropy pyrosilicates from the perspective of $\bar{r}(RE^{3+})$. The theoretical guidance makes it easier to synthesize high-entropy pyrosilicates with stable β-phase or γ-phase for the use in environmental barrier coatings (EBCs). The thermal expansion coefficient of γ-type high-entropy pyrosilicate can be altered through component design to match various types of CMCs.

Keywords: environmental barrier coatings (EBCs); high-entropy pyrosilicates; phase structure; thermal expansion coefficient (CTE)

* Corresponding author.
E-mail: zengyi@mail.sic.ac.cn

1 Introduction

Ceramic matrix composites (CMCs) are promising candidates to replace nickel-based alloys in the hot-end components of aero-engines. CMCs have excellent mechanical properties and low densities and can also withstand higher temperatures [1–3]. The key to increasing the specific core power of a gas turbine engine is to raise the inlet temperature [4]. Recently, the components prepared by SiC_f/SiC CMCs have been applied to GE9X engines [3]. However, at extremely high temperatures, SiC react with oxygen to form silicon scales, which then reacts with water vapor produced by fuel combustion to form $Si(OH)_4$ gas [5]. The long-term reaction leads to a sharp decline in the performance of CMCs [6,7]. The use of environmental barrier coating (EBC) is an important approach to enhancing the performance of CMCs at high temperatures [8]. In the case of EBC, a material coated on the surface of CMCs isolates the substrate from direct contact with the corrosive medium.

Rare-earth silicates (RE_2SiO_5 and $RE_2Si_2O_7$) are known as the preferred EBC materials [9,10]. The thermal expansion coefficients (CTEs) of β-type and γ-type pyrosilicates are about $(4.0–5.4)\times10^{-6}$ K^{-1} [11], which are very close to those of CMCs and Si bond layers, whose damage tolerance is excellent [12]. Therefore, EBC coatings made from these materials have exceptional thermal shock resistance. Among the single-component pyrosilicates, only $Yb_2Si_2O_7$, $Lu_2Si_2O_7$, and $Sc_2Si_2O_7$ can maintain a stable β-phase from room temperature to service temperature [13,14]. Moreover, there is no single-component pyrosilicate that can maintain γ-phase stability over the temperature range from room temperature to service temperature. The γ-phase only exists in the high-temperature sections of $Y_2Si_2O_7$, $Er_2Si_2O_7$, and $Ho_2Si_2O_7$ [13,14]. Nevertheless, the corrosion resistance of calcium magnesium aluminum silicate (CMAS) molten salt of $Yb_2Si_2O_7$, $Lu_2Si_2O_7$, and $Sc_2Si_2O_7$ is not enough to meet the service requirements [15,16]. Therefore, researchers focused on high-entropy pyrosilicates [17–20]. In Ref. [21], the high-entropy pyrosilicate with the largest average radius of the RE^{3+} ion was more likely to form a dense layer of apatite, resulting in improved CMAS corrosion resistance. However, the thermal expansion coefficient of traditional β-type pyrosilicate ($(4.0–5.4)\times10^{-6}$ K^{-1} [11]) is only comparable to that of SiC_f/SiC ($(4.5–5.9)\times10^{-6}$ K^{-1} [22]). The thermal expansion coefficient of β-type pyrosilicate is greater than those of C_f/SiC ($(2–3)\times10^{-6}$ K^{-1} [23]) and Si_3N_4 matrix composites ($(3–4)\times10^{-6}$ K^{-1} [24]), which may result in tensile stress of the coating during the thermal cycle and is not conducive to long-term service of the coating. Furthermore, in Refs. [17,18,20], RE element selection has been relatively blind. Still, the phase evolution of the obtained high-entropy pyrosilicates is unknown, and there is no universal rule for selecting RE elements for high-entropy pyrosilicates. If the contents of elements with large ionic radii are too high, pyrosilicate cannot maintain a stable β-phase or γ-phase, and the α-phase with a larger thermal expansion coefficient may form [11]. Therefore, the current study investigated a high-entropy pyrosilicate design method that can maintain the β-phase or γ-phase of pyrosilicates by regulating the average radius of RE^{3+} ions ($\bar{r}(RE^{3+})$). Simultaneously, component design has regulated the thermal expansion coefficient of pyrosilicate.

Herein, 12 kinds of high-entropy pyrosilicates with different compositions were synthesized via the solid-phase method. Their phase structures, phase stability, and thermal expansion coefficients were characterized and analyzed. Among them, nine kinds of high-entropy pyrosilicates formed β-phase or γ-phase. Meanwhile, the key factors affecting the phase structure of high-entropy pyrosilicates were discovered by comparing $\bar{r}(RE^{3+})$ and the cationic size difference (δ_r) of the as-synthesized pyrosilicates. The pyrosilicate gradually transformed from β-phase to γ-phase with an increase in the average radius of the RE^{3+} ion. The phase structures of these nine pyrosilicates are stable at room temperature to 1400 ℃. The thermal expansion coefficient is generally maintained at $(3–4)\times10^{-6}$ K^{-1}, which is very close to that of CMCs [22]. The average radius of the RE^{3+} ion was closely related to the phase structure of high-entropy pyrosilicates, and the CTE was closely related to the phase structure and the bond length of RE–O. The CTE of γ-type high-entropy pyrosilicate among 12 types of high-entropy pyrosilicate can vary within a certain range and can be changed in different directions to meet the requirements of different types of CMCs. The lowest obtained CTE is only $(2.43–3.32)\times10^{-6}$ K^{-1}, making it more suitable for Si_3N_4 matrix composites and C_f/SiC. During the thermal cycling process, the coating prepared from it could be subjected to less tensile stress or even only

compressive stress, which is better for the long-term service of ceramic coating. The component design of high-entropy pyrosilicates based on the average radius of the RE^{3+} ion promotes the directional regulation of the phase structure and thermal expansion coefficient. The current study not only broadens the family of high-entropy pyrosilicates but also lays the groundwork for developing EBCs that can be used in harsher environments.

2 Materials and methods

2. 1 Material synthesis

Raw materials included RE_2O_3 powders (RE = Sm, Eu, Gd, Dy, Y, Ho, Er, Tm, Yb, and Lu; $D_{50} \approx 5$ μm) and SiO_2 powders ($D_{50} \approx 28$ μm). 12 types of high-entropy pyrosilicate blocks with different compositions were prepared using the solid-phase method. The ratio of each RE_2O_3 to SiO_2 is the stoichiometric ratio. Ethanol and zirconia balls were used as the dispersion medium, and ball milling was performed for 12 h in a vertical nylon tank to ensure uniform mixing of the powders. The obtained slurry was dried at 120 ℃ for 5 h. After drying, the mixture was passed through a 20-mesh sieve. The sieved powders were placed in circular molds with diameter of 10 mm and cold pressed. Thereafter, the green billets were placed in a muffle furnace and maintained at 1600 ℃ for 10 h to obtain 12 types of high-entropy pyrosilicates.

2. 2 Characterization

The phase structures of high-entropy pyrosilicate blocks were determined by the X-ray diffractometer (D8 ADVANCE, Bruker, Germany). The X-ray diffraction (XRD) results were refined by using FullProf software to obtain accurate lattice parameters and atomic occupancies of different high-entropy pyrosilicates. The thermal behavior versus temperature was then studied by means of the *in situ* high-temperature X-ray diffractometer (D8 ADVANCE, Bruker, Germany) equipped with a heating system. The X-ray power is 40 kV and 40 mA; a 0.6 mm evanescent slit is used for data collection. The data were recorded over the 10°–70° 2θ range with a 5 (°)/min scan rate. The measurement temperature was from 27 to 1400 ℃ with a heating rate of 10 ℃/min, and the sample was held at each temperature for 15 min before scanning. The lattice parameters at different temperatures were obtained by using Jade 6.5 software. The anisotropic CTEs were determined by fitting the lattice parameter vs. temperature curves. Furthermore, high-entropy pyrosilicates were characterized by the scanning electron microscope (SEM; Magellan 400, FEI, USA) equipped with an energy dispersive X-ray spectrometer (Oxford, UK) to investigate the morphology and elemental composition in detail. An accelerating voltage of 20 kV was used to capture the energy dispersive X-ray spectroscopy (EDS) mappings. In addition, the phase stability of blocks was analyzed by a thermogravimetry/differential thermal analysis (TG/DTA) device (STA449C, NETZSCH, Germany), and the TG/DTA heating rate is 10 ℃/min. Furthermore, the thermal expansion coefficients of nine types of high-entropy pyrosilicates were measured by a thermal dilatometer (DIL 402SE, NETZSCH, Germany) during stepwise heating from room temperature to 1300 ℃ at a heating rate of 10 ℃/min. The CTE can be obtained by Eq. (1):

$$\mathrm{CTE} = \frac{\Delta L / L}{\Delta T} \tag{1}$$

where L is the length of the sample at room temperature, and ΔL and ΔT represent the change in length and temperature, respectively.

3 Results

3. 1 Micromorphology, composition, and phase structure

The 12 types of high-entropy pyrosilicates ($(Ho_{1/4}Er_{1/4}Yb_{1/4}Lu_{1/4})_2Si_2O_7$, $(Y_{1/6}Ho_{1/6}Er_{1/6}Tm_{1/6}Yb_{1/6}Lu_{1/6})_2Si_2O_7$, $(Y_{1/5}Ho_{1/5}Er_{1/5}Yb_{1/5}Lu_{1/5})_2Si_2O_7$, $(Dy_{1/5}Y_{1/5}Er_{1/5}Yb_{1/5}Lu_{1/5})_2Si_2O_7$, $(Gd_{1/6}Dy_{1/6}Ho_{1/6}Tm_{1/6}Yb_{1/6}Lu_{1/6})_2Si_2O_7$, $(Y_{1/4}Ho_{1/4}Er_{1/4}Tm_{1/4})_2Si_2O_7$, $(Gd_{1/4}Dy_{1/4}Yb_{1/4}Lu_{1/4})_2Si_2O_7$, $(Dy_{1/5}Y_{1/5}Ho_{1/5}Er_{1/5}Yb_{1/5})_2Si_2O_7$, $(Dy_{1/5}Y_{1/5}Ho_{1/5}Er_{1/5}Tm_{1/5})_2Si_2O_7$, $(Gd_{1/4}Dy_{1/4}Ho_{1/4}Er_{1/4})_2Si_2O_7$, $(Sm_{1/4}Eu_{1/4}Yb_{1/4}Lu_{1/4})_2Si_2O_7$, and $(Eu_{1/5}Gd_{1/5}Dy_{1/5}Y_{1/5}Ho_{1/5})_2Si_2O_7$) were labeled as HE-1–HE-12 according to the average radii of the RE^{3+} ions in the ascending order. The radii of different RE^{3+} ions and the average radii of the RE^{3+} ions in the high-entropy pyrosilicates are shown in Tables 1 and 2, respectively [25]. The surface morphologies and EDS elemental mappings of the 12 pyrosilicates are shown in Figs. 1 and 2, which indicate a relatively uniform distribution of various RE elements. The RE element contents of the whole plane scanning area in

Figs. 1 and 2 are shown in Table 3, which are very close to the theoretical value [26]. However, elemental segregation is clearly observed in the EDS elemental mappings of HE-10, HE-11, and HE-12.

Table 1 Radii of different RE^{3+} ions [25]

Type of RE^{3+}	Lu^{3+}	Yb^{3+}	Tm^{3+}	Er^{3+}	Ho^{3+}	Y^{3+}	Dy^{3+}	Gd^{3+}	Eu^{3+}	Sm^{3+}
Radius of RE^{3+} (Å)	1.032	1.042	1.052	1.062	1.072	1.075	1.083	1.107	1.120	1.132

Table 2 Average radii of RE^{3+} ions contained in HE-1–HE-12 [25]

Compound	HE-1	HE-2	HE-3	HE-4	HE-5	HE-6	HE-7	HE-8	HE-9	HE-10	HE-11	HE-12
$\bar{r}(RE^{3+})$ (Å)	1.0520	1.0558	1.0566	1.0588	1.0647	1.0653	1.0660	1.0668	1.0688	1.0810	1.0815	1.0914

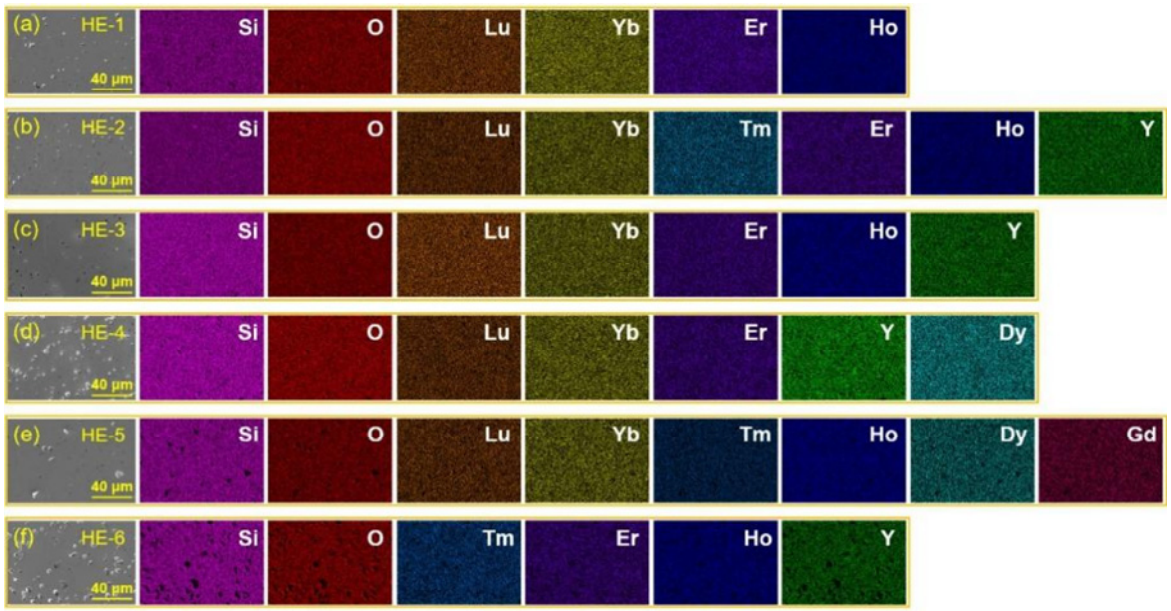

Fig. 1 SEM images and EDS elemental mappings of HE-1–HE-6.

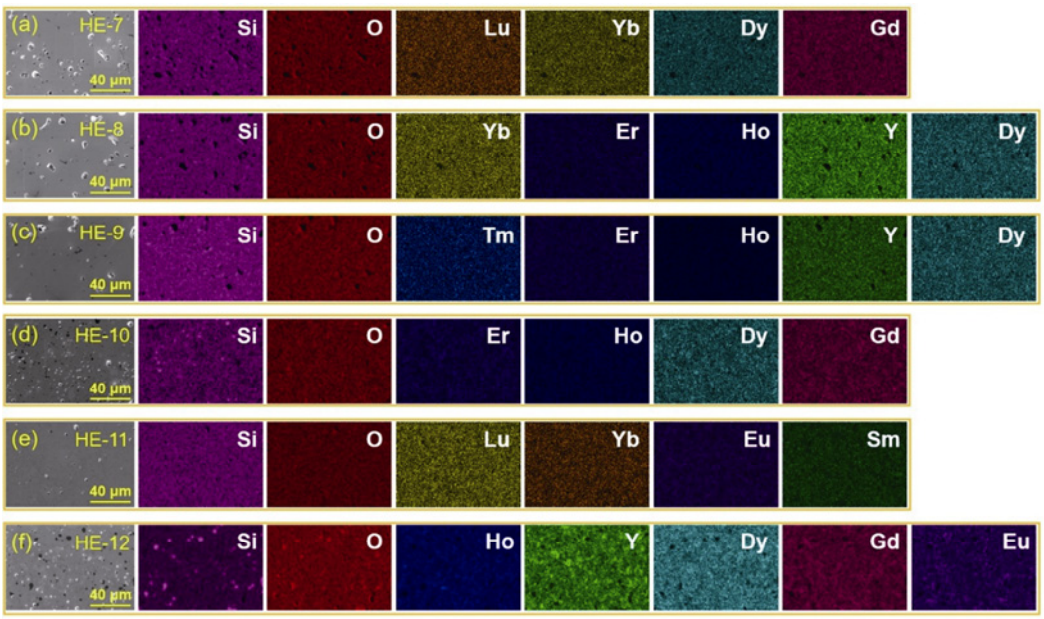

Fig. 2 SEM images and EDS elemental mappings of HE-7–HE-12.

Table 3 Element contents in the scanning areas of HE-1–HE-12 (Unit: %)

Element	HE-1	HE-2	HE-3	HE-4	HE-5	HE-6	HE-7	HE-8	HE-9	HE-10	HE-11	HE-12
O	63.62	63.65	63.63	63.65	63.62	63.57	63.70	63.63	63.58	63.60	63.74	63.72
Si	18.09	18.22	18.15	18.26	18.18	17.78	18.43	18.14	17.87	18.00	18.65	18.53
Sm	—	—	—	—	—	—	—	—	—	—	3.95	—
Eu	—	—	—	—	—	—	—	—	—	—	4.58	3.60
Gd	—	—	—	—	3.14	—	4.62	—	—	4.99	—	3.91
Dy	—	—	—	3.71	2.73	—	4.40	3.63	3.20	4.31	—	3.11
Y	—	3.24	3.64	3.71	—	4.80	—	3.51	4.09	—	—	3.53
Ho	4.30	2.78	3.38	—	3.13	4.35	—	3.49	3.46	4.33	—	3.60
Er	4.84	2.92	3.83	3.54	—	4.55	—	3.89	3.66	4.77	—	—
Tm	—	2.95	—	—	2.86	4.95	—	—	4.14	—	—	—
Yb	4.49	3.19	3.61	3.32	3.13	—	4.10	3.71	—	—	4.34	—
Lu	4.66	3.05	3.76	3.81	3.21	—	4.75	—	—	—	4.74	—
Total	100.00	100.00	100.00	100.00	100.00	100.00	100.00	100.00	100.00	100.00	100.00	100.00

Figure 3 shows the XRD patterns of 12 different kinds of high-entropy pyrosilicates, in which HE-1–HE-4 show a β-phase, and their diffraction peaks are consistent with the card of PDF#25-1345 (β-$Yb_2Si_2O_7$). HE-5 and HE-7–HE-9 show a γ-phase, and their diffraction peaks are consistent with the card of PDF#42-0167 (γ-$Y_2Si_2O_7$). The main phase of HE-6 is the γ-phase, but the β-phase also exists as a secondary phase. The diffraction peaks of the four single β-phase and four single γ-phase pyrosilicates gradually move to small angles as $\bar{r}(RE^{3+})$ increases. However, HE-10, HE-11, and HE-12 did not form a single β-phase or γ-phase. The main diffraction peak of HE-10 is consistent with the α-type pyrosilicate, and its diffraction peaks are consistent with the card of PDF#24-0065 (α-$Gd_2Si_2O_7$). Moreover, the diffraction peaks of α-phase and β-phase pyrosilicates were detected in the XRD pattern of HE-12. The diffraction peaks of HE-11 are relatively disordered due to the existence of seven types of crystals in pyrosilicate. It is difficult to determine which phases HE-11 contains, but it can be determined that there are phases other than β-phase and γ-phase.

The XRD results of seven types of β-type or γ-type high-entropy pyrosilicates were refined by using Fullprof software, and HE-6 was refined for both β-phase and γ-phase. The XRD refined results of HE-2 (β-phase), HE-5 (γ-phase), and HE-6 (both β and γ phases) are shown in Fig. 4. The XRD refined results of other high-entropy pyrosilicates are shown in Fig. S1 in the Electronic Supplementary Material (ESM). The data for HE-1 and HE-3 were obtained from Ref. [21]. Table 4 displays the lattice parameters (*a*, *b*, and *c*) obtained for nine types of β-type or γ-type high-entropy pyrosilicates. Among them, HE-6 contains 71.45% γ-phase and 28.55% β-phase. Figure 4(d) shows that the cell volumes (*V*) of four single β-phase (HE-1–HE-4) and four single γ-phase (HE-5 and HE-7–HE-9) pyrosilicates gradually increase as $\bar{r}(RE^{3+})$ increases.

According to the structures of pyrosilicates (Fig. 5), the structures of β-type and γ-type are similar. In both the structures, RE ions bonded with the adjacent six oxygen atoms, while Si atoms bonded with the adjacent four oxygen atoms. The space group of β-pyrosilicate is C_2/m, its crystal is composed of $[Si_2O_7]^{6-}$ units, and RE ions stacked along the *b*-axis. The $[Si_2O_7]^{6-}$ unit consists of two $[SiO_4]^{4-}$ tetrahedra connected at the top corners. The space group of γ-type pyrosilicate is $P2_1/b$, and its structure is very similar to that of β-type pyrosilicate. However, the $[Si_2O_7]^{6-}$ units in the crystal are stacked with RE ions in a sine-wave pattern. The phase transition between β-phase and γ-phase does not involve bond breaking and re-bonding. The bond length data obtained by refinement and the deformation degree (Δd) of $[SiO_4]^{4-}$ tetrahedron and $[REO_6]^{9-}$ octahedron are shown in Tables 5 and 6. Δd is calculated by Eq. (2):

$$\Delta d = \frac{1}{n}\sum_{i=1}^{n}\left(\frac{d(\mathrm{L-O})_i - \overline{d(\mathrm{L-O})}}{\overline{d(\mathrm{L-O})}}\right)^2 \quad (2)$$

where $d(\mathrm{L-O})_i$ is the distance of L–O (L = RE or Si) between the *i*-th O atom and the L atom, and $\overline{d(\mathrm{L-O})}$ is the average L–O distance. The RE–O

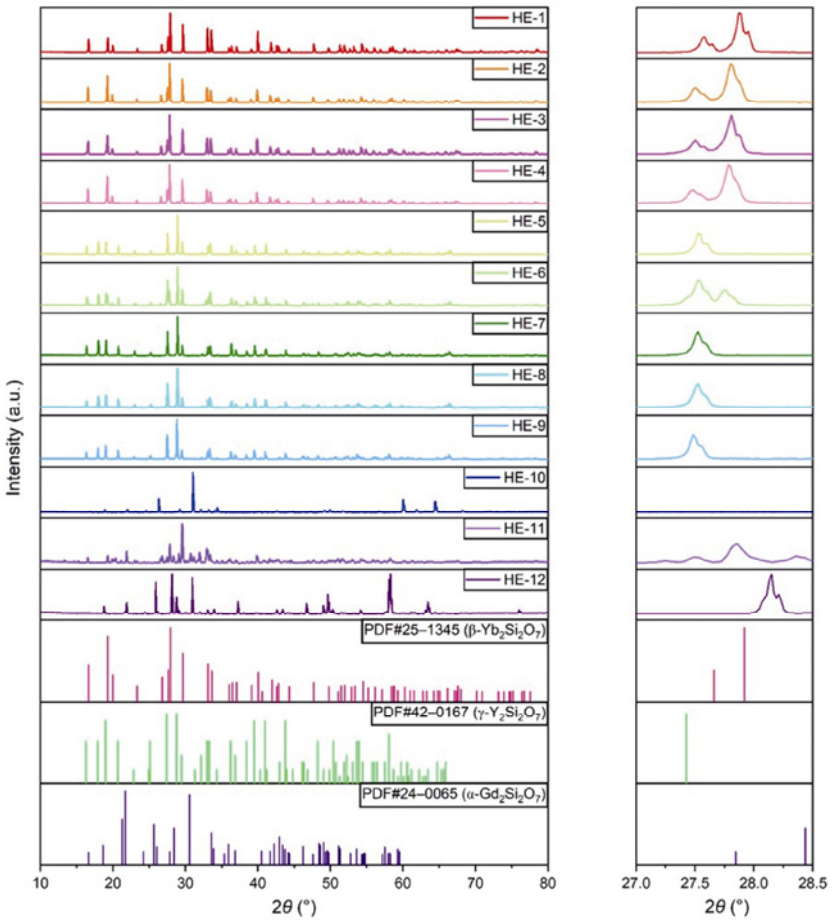

Fig. 3 XRD patterns of 12 types of high-entropy pyrosilicates.

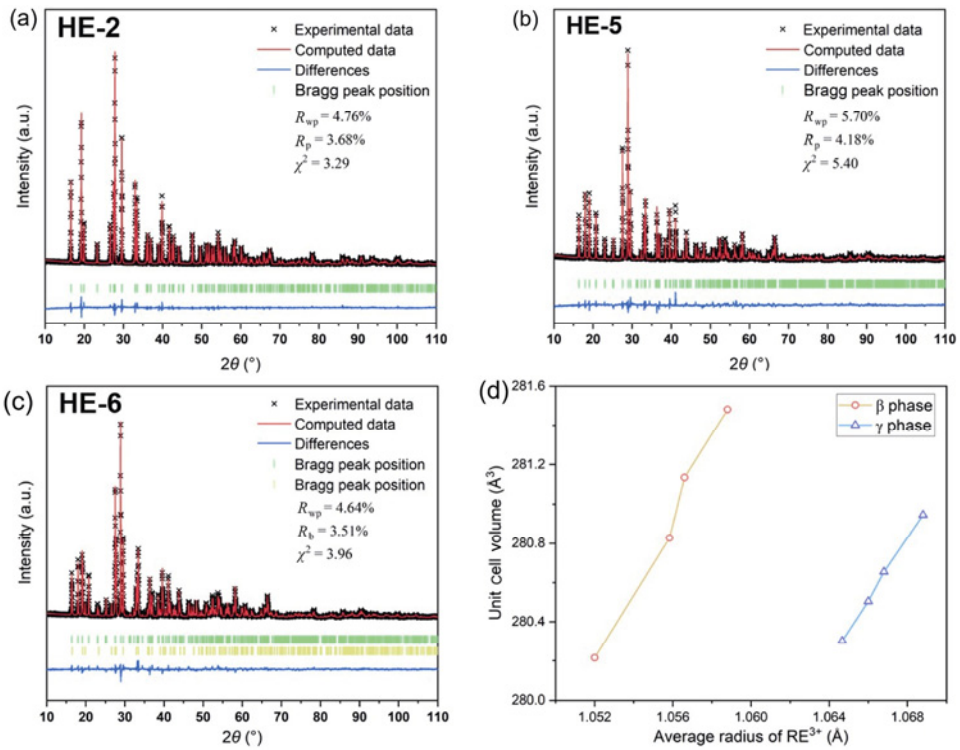

Fig. 4 (a–c) Rietveld refinements of the XRD patterns of three high-entropy pyrosilicates and (d) variations of V with $\bar{r}(RE^{3+})$.

Table 4 Crystal cell parameters obtained by the XRD-Rietveld refinement, measured densities, and relative densities of nine β- or γ-type pyrosilicates

Compound	R_p (%)	R_{wp} (%)	a (Å)	b (Å)	c (Å)	V (Å^3)	β (°)	Phase	Measured density (g/cm^3)	Relative density (%)
HE-1 [16]	4.25	5.54	6.8214	8.9017	4.7152	280.215	101.848	β	5.80	96.28
HE-2	3.30	4.26	6.8322	8.9131	4.7119	280.828	101.841	β	5.61	98.61
HE-3 [16]	4.21	5.69	6.8316	8.9152	4.7161	281.134	101.822	β	5.32	94.73
HE-4	3.51	4.64	6.8381	8.9190	4.7151	281.481	101.811	β	5.49	92.11
HE-5	5.70	4.18	4.6841	10.8137	5.5645	280.303	96.011	γ	5.56	93.44
HE-6	4.64	3.51	6.8552	8.9427	4.7181	283.170	101.759	β (28.55%)	4.73	—
HE-6	4.64	3.51	4.6865	10.8070	5.5653	280.298	96.043	γ (71.45%)	4.73	—
HE-7	4.20	3.20	4.6843	10.8205	5.5644	280.505	95.986	γ	5.42	91.20
HE-8	4.14	3.20	4.6865	10.8159	5.5676	280.655	96.027	γ	5.22	93.68
HE-9	4.09	3.14	4.6853	10.8226	5.5712	280.946	96.016	γ	5.23	94.38

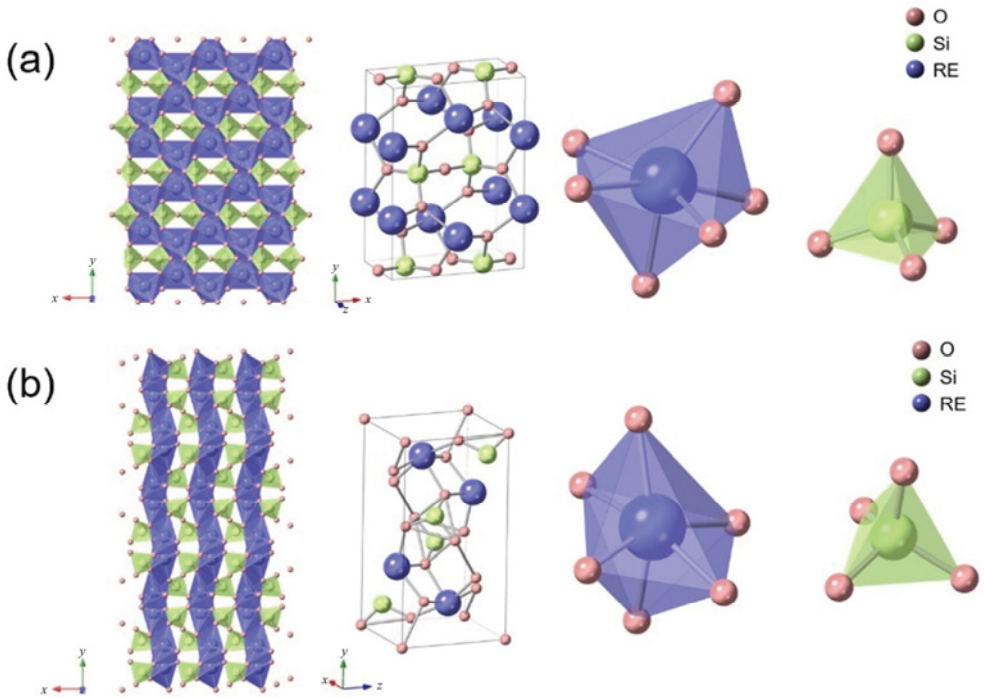

Fig. 5 Crystal structures of (a) β-type and (b) γ-type pyrosilicates.

Table 5 RE–O and Si–O bond lengths and Δd of $[REO_6]^{9-}$ octahedron and $[SiO_4]^{4-}$ tetrahedron units in β-type pyrosilicates

Compound	Bond	Site	Bond length (Å)						Average bond length (Å)	Δd (‰)
HE-1 [21]	RE–O	$[REO_6]$	2.228	2.228	2.258	2.258	2.279	2.279	2.255	0.0861
	Si–O	$[SiO_4]$	1.577	1.623	1.640	1.640	—	—	1.620	0.2532
HE-2	RE–O	$[REO_6]$	2.204	2.204	2.239	2.239	2.277	2.277	2.240	0.1771
	Si–O	$[SiO_4]$	1.619	1.672	1.636	1.636	—	—	1.641	0.1388
HE-3 [21]	RE–O	$[REO_6]$	2.212	2.212	2.307	2.307	2.315	2.315	2.278	0.4218
	Si–O	$[SiO_4]$	1.647	1.650	1.559	1.559	—	—	1.604	0.7790
HE-4	RE–O	$[REO_6]$	2.214	2.214	2.228	2.228	2.312	2.312	2.251	0.3695
	Si–O	$[SiO_4]$	1.633	1.653	1.618	1.618	—	—	1.631	0.0776
HE-6	RE–O	$[REO_6]$	2.222	2.222	2.284	2.284	2.387	2.387	2.298	0.8772
(β phase)	Si–O	$[SiO_4]$	1.638	1.643	1.530	1.530	—	—	1.585	1.2159

Table 6 RE–O and Si–O bond lengths and Δ*d* of $[REO_6]^{9-}$ octahedron and $[SiO_4]^{4-}$ tetrahedron units in γ-type pyrosilicates

Compound	Bond	Site	Bond length (Å)						Average bond length (Å)	Δ*d* (‰)
HE-6	RE–O	$[REO_6]$	2.093	2.097	2.174	2.210	2.231	2.359	2.144	2.3274
(γ phase)	Si–O	$[SiO_4]$	1.670	1.677	1.802	1.820	—	—	1.742	1.5725
HE-5	RE–O	$[REO_6]$	1.832	1.864	2.111	2.140	2.336	2.660	1.987	27.5801
	Si–O	$[SiO_4]$	1.699	1.768	2.035	2.123	—	—	1.906	8.6427
HE-7	RE–O	$[REO_6]$	1.854	2.017	2.084	2.261	2.267	2.548	2.054	14.7954
	Si–O	$[SiO_4]$	1.648	1.845	1.880	2.014	—	—	1.847	5.0273
HE-8	RE–O	$[REO_6]$	1.906	2.088	2.147	2.168	2.354	2.477	2.077	10.7739
	Si–O	$[SiO_4]$	1.688	1.806	1.810	1.846	—	—	1.788	1.1088
HE-9	RE–O	$[REO_6]$	1.984	2.037	2.179	2.206	2.250	2.308	2.102	3.7583
	Si–O	$[SiO_4]$	1.668	1.754	1.850	1.904	—	—	1.794	2.541

bond length of β-type pyrosilicate is generally greater than that of γ-type pyrosilicate, while the Si–O bond length of β-type pyrosilicate is generally smaller than that of γ-type pyrosilicate. Δ*d* of $[SiO_4]^{4-}$ tetrahedron and $[REO_6]^{9-}$ octahedron of γ-type pyrosilicate are much larger than that of β-type pyrosilicate.

3.2 Thermal stability and thermal expansion coefficient

The TG/DTA curves of HE-2 (β-phase) and HE-5 (γ-phase) are shown in Fig. 6. The TG/DTA curves of the other high-entropy pyrosilicates are shown in Fig. S2 in the ESM. As the temperature increased from room temperature to service temperature, the quality did not decrease considerably; however, the DTA signals showed some fluctuations, as shown in Fig. 6 and Fig. S2 in the ESM. To further explore the stability of the β- and γ-phases during the heating process, the XRD patterns of different high-entropy pyrosilicates were tested at different temperatures. Figure 7 shows the XRD patterns of HE-2 (β-phase) and HE-5 (γ-phase) at different temperatures. In Fig. 7, both HE-2 and HE-5 retain their original β-phase or γ-phase stably throughout the temperature range (from room temperature to 1400 ℃).

Figure 8 shows the curves of thermal expansion rates (dL/L_0) and CTEs of HE-1–HE-9 for the temperature range from 200 to 1300 ℃ obtained by the thermal dilatometer. Figure 8(c) shows the CTEs of β-type pyrosilicates (HE-1–HE-4), which are similar. Figure 8(d) shows the CTEs of γ-type pyrosilicates (HE-5 and HE-7–HE-9), which fluctuate within a certain range. In Table 7, the CTEs of HE-1–HE-9 are shown from 200 to 1300 ℃.

As shown in Figs. 9(a) and 9(b), the cell parameters of HE-2 (β-type) and HE-5 (γ-type) were obtained at different temperatures by processing the XRD patterns at different temperatures (Fig. 7) by using Jade 6.5 software. *a*, *b*, *c*, and *V* steadily increased from 27 to 1400 ℃. The volumetric CTE (α_V) is calculated by Eq. (3) [27]:

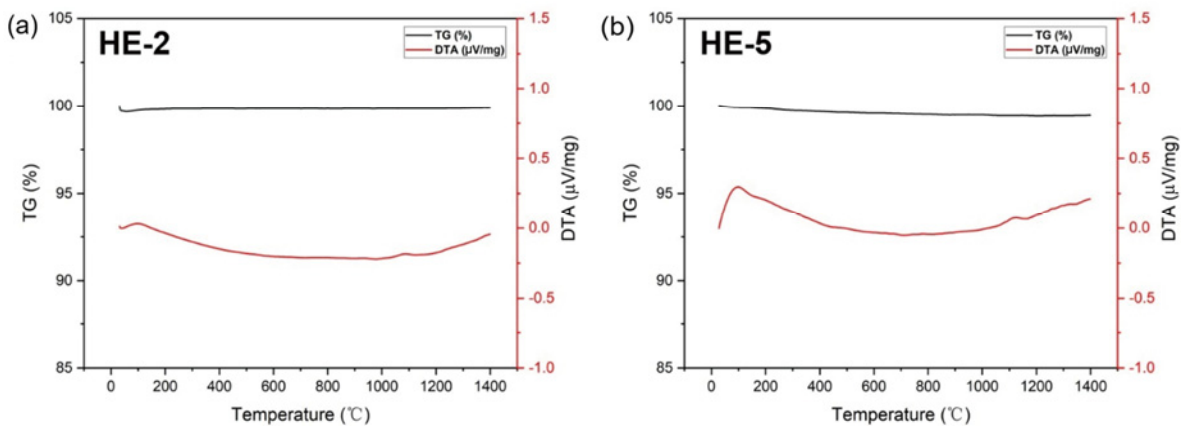

Fig. 6 TG/DTA curves of (a) HE-2 (β-phase) and (b) HE-5 (γ-phase).

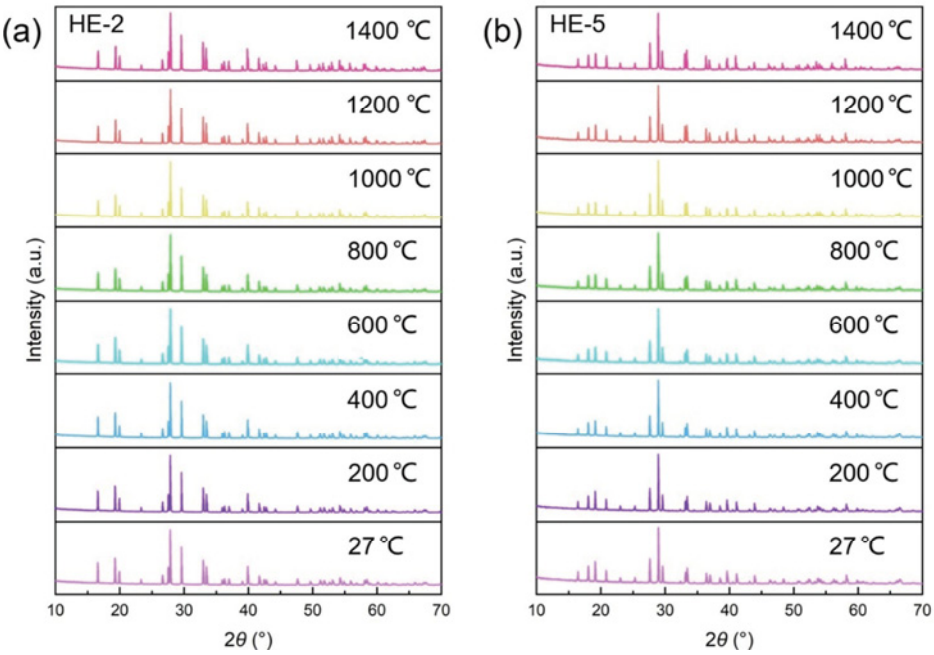

Fig. 7 XRD patterns of (a) HE-2 (β-phase) and (b) HE-5 (γ-phase) at different temperatures.

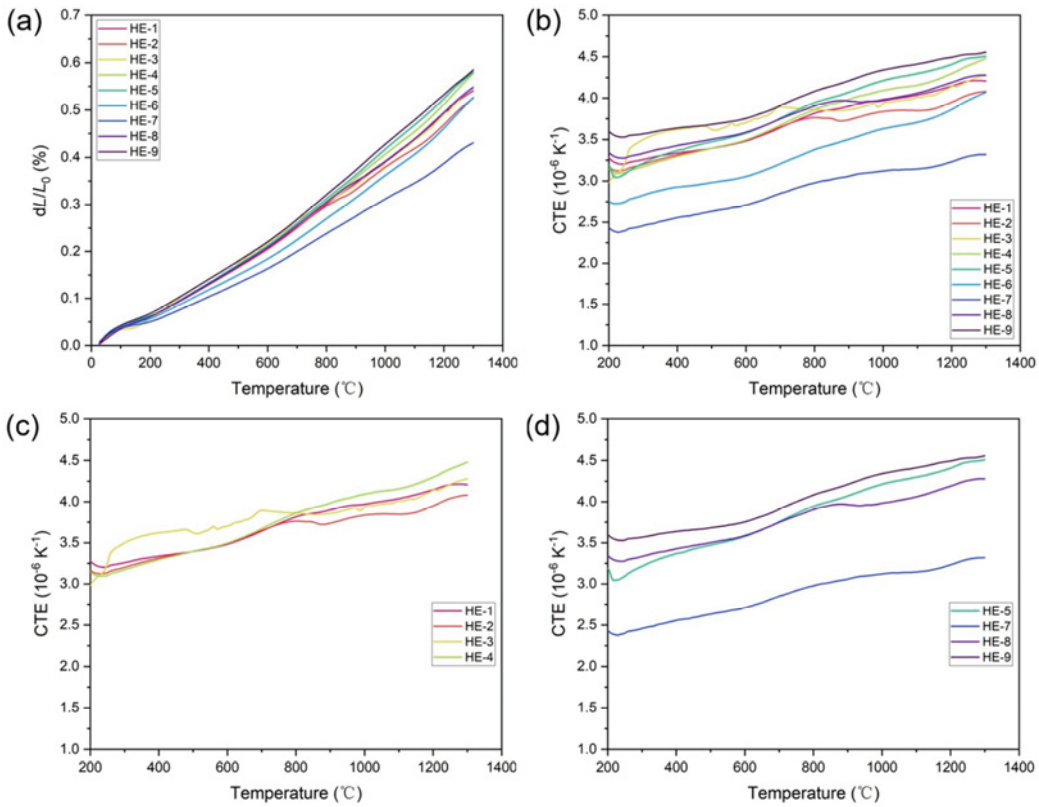

Fig. 8 (a) dL/L_0 of HE-1–HE-9, (b) CTEs of HE-1–HE-9, (c) CTEs of β-type pyrosilicates, and (d) CTEs of γ-type pyrosilicates. All data are determined using a thermal dilatometer.

Table 7 CTEs of HE-1–HE-9 from 200 to 1300 ℃

Compound	HE-1	HE-2	HE-3	HE-4	HE-5	HE-6	HE-7	HE-8	HE-9
CTE (10^{-6} K^{-1})	3.28–4.21	3.17–4.08	2.98–4.28	3.15–4.48	3.19–4.51	2.75–4.07	2.43–3.32	3.34–4.28	3.60–4.56

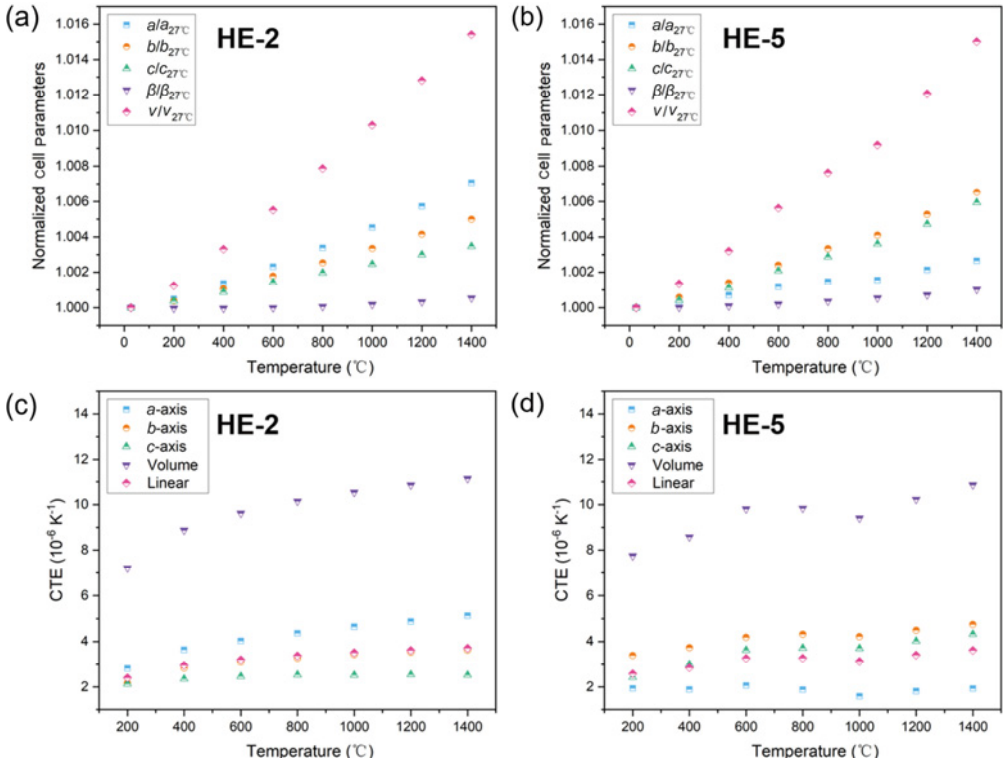

Fig. 9 Variations of normalized *a*, *b*, and *c* and anisotropic CTEs of (a, c) HE-2 (β-type) and (b, d) HE-5 (γ-type) with temperature by the high-temperature X-ray diffraction (HTXRD).

$$\alpha_V = \frac{1}{V\left(\frac{\partial V}{\partial T}\right)_P} \qquad (3)$$

$$V(T) = V_0 \exp\left(\int \alpha_V(T) \mathrm{d}T\right)$$

where V_0 is the volume at 27 ℃, and $\alpha_V(T)$ is a temperature-dependent CTE. When the temperature was higher than the Debye temperature, $\alpha_V(T) = \alpha_V$, and the equation can be simplified by Eq. (4) [27]:

$$\ln\left(\frac{V}{V_0}\right) = \alpha_V \left(T - T_0\right) \qquad (4)$$

The axial, volumetric, and linear CTEs of HE-2 (β-type) and HE-5 (γ-type) (Figs. 9(c) and 9(d), respectively) are calculated by *a*, *b*, and *c* at different temperatures. HE-2 (β-type) and HE-5 (γ-type) possess anisotropic CTEs. The axial CTEs of *a*-axis (α_a) were the highest among the three axes of β-type pyrosilicates, while the highest anisotropic CTEs of γ-type pyrosilicates were the axial CTEs of the *b*-axis (α_b). The linear CTEs were one-third of α_V. The linear CTE of HE-2 (β-type) was slightly higher than that of HE-5 (γ-type).

The data in the plot of $\ln\left(\frac{V}{V_0}\right)$ (as well as $\ln\left(\frac{a}{a_0}\right)$, $\ln\left(\frac{b}{b_0}\right)$, and $\ln\left(\frac{c}{c_0}\right)$) and $T - T_0$ were linearly fitted, and the α_V, α_a, α_b, and α_c of HE-2 (β-type) were determined to be 10.67×10^{-6}, 4.77×10^{-6}, 3.47×10^{-6}, and 2.52×10^{-6} K^{-1}, respectively. Similarly, the calculated α_V, α_a, α_b, and α_c of HE-5 (γ-type) were 10.18×10^{-6}, 1.84×10^{-6}, 4.47×10^{-6}, and 3.98×10^{-6} K^{-1}, respectively. To demonstrate the anisotropic thermal expansion, the variation of CTE as a function of crystal orientation was considered.

To demonstrate the anisotropic CTEs of the β- and γ-type pyrosilicates, the change in CTE as a function of crystal orientation was considered. The *x*-axis, *y*-axis, and *z*-axis were chosen as the coordinate axes. The CTE in an arbitrary direction (α') is expressed by Eq. (5) [28]:

$$\alpha' = \alpha_x \cos^2\varphi \sin^2\theta + \alpha_y \sin^2\varphi \sin^2\theta + \alpha_z \cos^2\theta \qquad (5)$$

where α_x, α_y, and α_z are the CTEs along the principal axes, and φ and θ are the azimuth and elevation angles of spherical coordinates, respectively.

Equation (6) should be satisfied.

$$\alpha_V = \alpha_x + \alpha_y + \alpha_z \qquad (6)$$

In a monoclinic crystal, α_x, α_y, and α_z were approximated as follows: The *b*-axis was perpendicular

to the *a*-axis and *c*-axis, i.e., $\alpha_y = \alpha_b$. α_x and α_z were approximated as follows: The *x*-axis direction was assumed to coincide with the *a*-axis direction, and we assumed that the angle between the *z*-axis and *c*-axis is β'. Equations (7) and (8) are satisfied:

$$\alpha_x = \alpha_a - \alpha_c \sin\beta' \quad (7)$$

$$\alpha_z = \alpha_c \cos\beta' \quad (8)$$

Thus, the CTEs along the *x*-axis and *z*-axis are obtained by Eq. (6). Using the calculated α_x, α_y, and α_z, the variation of CTE is obtained by Eq. (5). The spatial contours of the coefficients of thermal expansion coefficients of the two types of pyrosilicates are shown in Fig. 10. The two types of pyrosilicates exhibited different anisotropic thermal expansion coefficients.

4 Discussion

4.1 Phase structure

Among the single-component pyrosilicates, only $Yb_2Si_2O_7$, $Lu_2Si_2O_7$, and $Sc_2Si_2O_7$ can maintain a stable β-phase within the whole temperature range. The other single-component pyrosilicates showed phase transformation during the heating process [11,12], but the elements other than Yb, Lu, and Sc (elements with larger ionic radius, such as the Y element) can provide better corrosion resistance for EBC [14,16]. Therefore, the high-entropy design of RE pyrosilicates through the introduction of RE^{3+} ions with larger radii on the basis of suppressing the high-temperature phase transition could be the key breakthrough direction of RE pyrosilicates applied to EBCs. In the present study, the crystal type of high-entropy pyrosilicate gradually changes from β-type to γ-type with an increase in $\bar{r}(RE^{3+})$, but the continuous increase in $\bar{r}(RE^{3+})$ after a certain limit produces other types of crystal with incompatible thermal expansion coefficients, as shown in Fig. 11. When $\bar{r}(RE^{3+}) \leqslant 1.0588$ Å, the high-entropy pyrosilicate exhibits β-phase. When 1.0647 Å $\leqslant \bar{r}(RE^{3+}) \leqslant 1.0688$ Å, high-entropy pyrosilicates show γ-phase. The exception is HE-6, composed of the elements with close ionic radii (Tm, Er, Ho, and Y). In the case of HE-6, γ-phase is formed as the main phase, but a 28.55% β-phase is also formed. On the other hand, the β-phase is formed in HE-2, which is composed of the four elements (Tm, Er, Ho, and Y) along with Yb and Lu having smaller ionic radii. While the γ-phase is formed in HE-9, which is composed of the four elements (Tm, Er, Ho, and Y) along with Dy having a larger ionic radius, indicating the capability of these four elements (Tm, Er, Ho, and Y) to form a single phase. And the six-component HE-5 with the smaller average radius RE^{3+} ion forms a single γ-phase. The formation of a single γ-phase is thought to be caused by insufficient mixing entropy (ΔS_{mix}) of HE-6. ΔS_{mix} of high-entropy compounds with different numbers of components are calculated by Eq. (9):

$$\Delta S_{mix} = k_B \ln\Omega = -N_A k_B \sum_{i=1}^{n} x_i \ln x_i = N_A k_B \ln n \quad (9)$$

ΔS_{mix} of HE-5 is 14.896 J/(mol·K), while that of HE-6 is only 11.526 J/(mol·K). In the high-temperature segments of $Y_2Si_2O_7$, $Er_2Si_2O_7$, and $Ho_2Si_2O_7$, the γ-phase exists at a higher temperature than the β-phase [13]. Although both the segments belong to the monoclinic system, the γ-phase has higher symmetry than the β-phase [29]. The mixing enthalpy (ΔH_{mix}) required for the γ-phase transition is greater than that for the β-phase transition. As shown in Eq. (10), high ΔS_{mix} can provide a driving force for the high-temperature

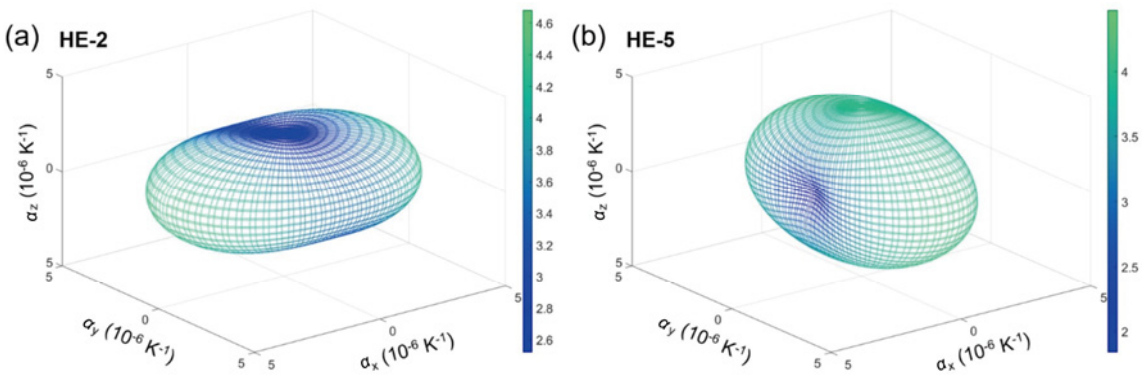

Fig. 10 Spatial contours of thermal expansion coefficients of (a) HE-2 (β-type) and (b) HE-5 (γ-type).

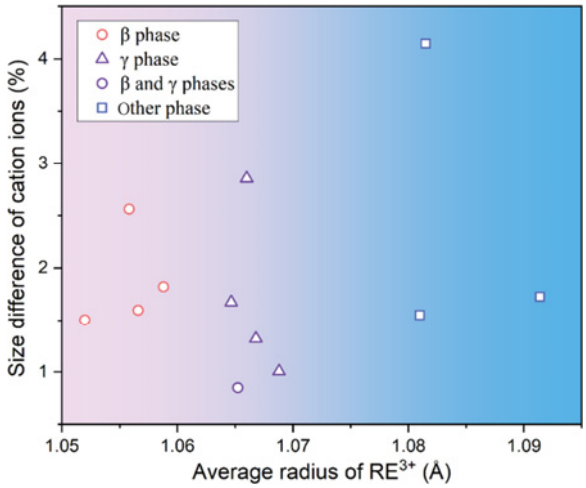

Fig. 11 $\bar{r}(RE^{3+})$ and size differences of cations of 12 high-entropy pyrosilicates.

phase to move toward the low temperature (when the mixing Gibbs free energy (ΔG_{mix}) is less than zero), so the high-temperature phase can exist stably at a low temperature [30].

$$\Delta G_{mix} = \Delta H_{mix} - T\Delta S_{mix} < 0 \quad (10)$$

ΔS_{mix} of four-component HE-6 is smaller than that of six-component HE-5, and ΔS_{mix} of HE-6 may not be enough to provide the driving force for the transformation of the remaining 28.55% β-phase to γ-phase.

The atomic size difference (δ) is one of the important composition-weighted terms used in high-entropy materials [31]. Typically, systems with low size differences are more likely to form a single phase. In the present study, RE elements exist in the form of ions with +3 charge, and the cation size difference is used to describe the deviation degree of the cation radius of different RE elements. δ_r is calculated by Eq. (11):

$$\delta_r = \sqrt{\sum c_i \left(1 - r_i / \bar{r}\right)^2} \quad (11)$$

where r_i and c_i are the cationic radius and cation fraction of an element i, respectively, and $\bar{r}$ is the average cationic radius. In the present work, no clear relationship has been observed between δ_r and the formation of a single phase. HE-6 had the smallest δ_r but did not form a single phase, while HE-2 and HE-7 had a larger δ_r but formed a single phase, as shown in Fig. 11. Therefore, compared with the average radius of the RE^{3+} ion and the number of components, δ_r may not be an important reference criterion for obtaining single-phase high-entropy pyrosilicates.

4. 2 Thermal expansion coefficient

References [32–34] show that the average thermal expansion coefficient (α) of Si–O bonds is about 0.0 K^{-1}. The average thermal expansion of the RE–O bond can be estimated according to the Hazen and Prewitt model [35]. They found the equation for the determination of the α for metal–oxygen bonds, which is valid for oxides and silicates, as shown in Eq. (12):

$$\alpha = 32.9\left(0.75 - \frac{z}{p}\right) \times 10^{-6} K^{-1} \quad (12)$$

where z is the cation charge number, and p is the cation coordination number. The thermal expansion coefficient of the RE–O bonds of both β-type and γ-type pyrosilicates is found to be equal to 8.2. The $RE_2Si_2O_7$ crystal structure basically expands along the $[REO_x]$ polyhedron chain [11]. Therefore, the thermal expansion coefficient of pyrosilicate is mainly attributed to the stretching vibration of the RE–O bond and has little association with the Si–O bond.

The thermal expansion coefficient is proportional to the spacing between atoms in the lattice and inversely proportional to the lattice energy [36]. Figure 12 shows the average RE–O bond lengths (the spacing of atoms) for the four single-phase β-type pyrosilicates and γ-type pyrosilicates, as plotted from the data in Tables 5 and 6. The average length of RE–O bond in β-type pyrosilicate varies only slightly with $\bar{r}(RE^{3+})$. Moreover, the six RE–O bonds of the $[REO_6]^{9-}$ octahedron are similar in length, so the distortion rate (Δd) of $[REO_6]^{9-}$ octahedron is very small. This could explain why the thermal expansion coefficients of β-type pyrosilicates are comparable. This finding is also consistent with that reported in Ref. [11], which found that the thermal expansion coefficient of β-type pyrosilicate is only related to the crystal type, and has little to do with the RE element. However, compared with that of β-type pyrosilicates, the average RE–O bond length of γ-type pyrosilicates varies significantly with the average radius of the RE^{3+} ion, which may result in the fluctuation of the thermal expansion coefficient of γ-type pyrosilicates within a certain range, as shown in Fig. 8(d). The thermal expansion coefficients of HE-7–HE-9 are correlated with the average RE–O bond length, as shown in Fig. 13. However, the γ-phase HE-5 exhibits an abnormally increased thermal expansion coefficient, which does not match its average RE–O bond. HE-5 had the highest number of RE elements in the solid solution (6).

The lattice distortion effect of the high-entropy ceramics may be the reason for the Δd of the $[REO_6]^{9-}$ octahedron being as high as 27.5801‰. As a result, the bond lengths of the six RE–O bonds of HE-5 vary greatly. The bond length of the No. 1 bond is the longest of all the γ-type pyrosilicates, as shown in Fig. 14. The vectors of the six bonds represented by the *a*-axis, *b*-axis, and *c*-axis as unit vectors are shown in Table 8. Among them, the longest No. 1 bond has the largest projection on the *b*-axis among the three axes. Also, the No. 1 bond has the largest projection on the *b*-axis among all the bonds. The atomic arrangements of the $[REO_6]^{9-}$ octahedron in the [001] direction are shown in Fig. 14. The connection between RE and O atoms by the No. 1 bond makes the chain of $[REO_6]^{9-}$ octahedrons extend in the *b*-axis direction. Therefore, the increase of *b*-axis lattice parameters is closely related to the elongation of the No. 1 bond. The HTXRD results of HE-5 were refined by using FuffProf software to obtain RE–O bond lengths and Δd of $[REO_6]^{9-}$ octahedron units at different temperatures, as shown in Table 9. The bond lengths showed an overall elongation trend with the increasing temperature, and the distortion was all maintained at a high value. As shown in Fig. 10, β-type and γ-type pyrosilicates exhibit different anisotropic thermal expansion phenomena. As shown in Fig. 9, the anisotropic CTEs of the three axial β-type pyrosilicates are *a*-axis, *b*-axis, and *c*-axis from large to small. While the anisotropic CTE of *b*-axis is the largest among the three axes of γ-type pyrosilicates. As a result, the elongation of lattice parameters along the *b*-axis contributes the most to the thermal expansion coefficient of γ-type pyrosilicates.

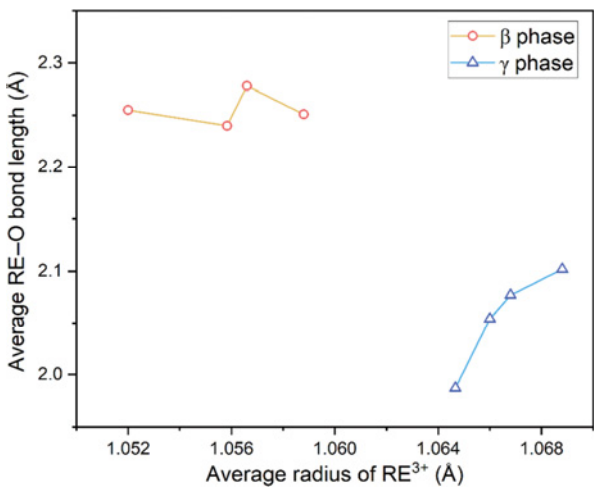

Fig. 12 Average RE–O bond lengths of the eight single-phase pyrosilicates.

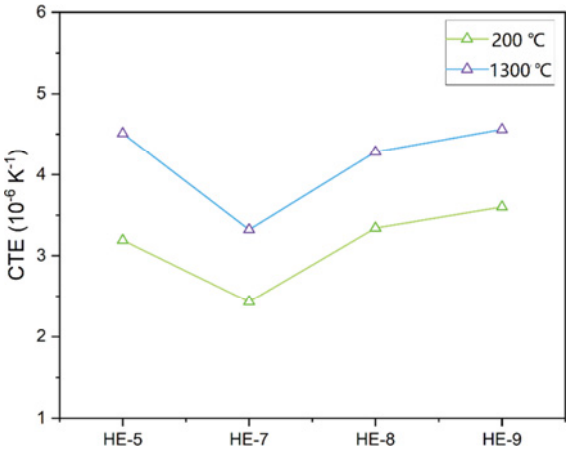

Fig. 13 CTEs of γ-type pyrosilicates at 200 and 1300 ℃ via the thermal dilatometer.

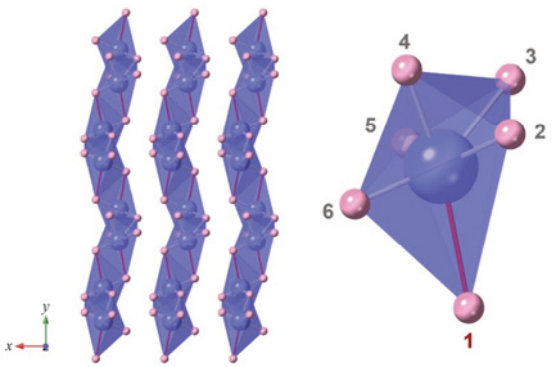

Fig. 14 Arrangements of $[REO_6]^{9-}$ octahedron of HE-5 along the [001] direction and six RE–O bonds of $[REO_6]^{9-}$ octahedron.

HE-5 with the longest No. 1 bond and the high Δd of the $[REO_6]^{9-}$ octahedron may be responsible for obtaining a higher thermal expansion coefficient. The thermal expansion coefficients of various CMCs are similar, but there is still a certain gap. The thermal expansion coefficients of C_f/SiC, Si_3N_4, and SiC_f/SiC are (2–3)×10^{-6} K^{-1} [23], (3–4)×10^{-6} K^{-1} [24], and (4.5–5.9)×10^{-6} K^{-1} [22], respectively. As a result, the thermal expansion coefficient of γ-type pyrosilicate can be matched with different CMCs via composition design.

Table 8 Vectors of six bonds represented by *a*-axis, *b*-axis, and *c*-axis as unit vectors in HE-5

RE–O bond number	$\vec{a}$	$\vec{b}$	$\vec{c}$	Bond length (Å)
No. 1	0.107	0.237	0.100	2.660
No. 2	0.269	−0.054	0.311	2.111
No. 3	0.269	−0.146	−0.189	2.336
No. 4	−0.133	−0.161	0.182	2.140
No. 5	−0.133	−0.039	−0.319	1.864
No. 6	−0.335	0.063	0.092	1.832

Note: The bond numbers are derived from Fig. 14.

Table 9 RE–O bond lengths and Δd of $[REO_6]^{9-}$ octahedron units in HE-5 at different temperatures obtained using FullProf refinement

Temperature (℃)	RE–O bond length (Å)						Average bond length (Å)	Δd (‰)
27	1.803	2.013	2.048	2.205	2.479	2.627	2.196	16.4456
200	1.780	1.999	2.093	2.237	2.397	2.670	2.196	16.9083
400	1.967	1.974	1.984	2.345	2.468	2.508	2.208	11.6057
600	1.861	2.013	2.028	2.338	2.426	2.680	2.224	16.0494
800	1.971	2.007	2.073	2.354	2.409	2.597	2.235	10.7889
1000	1.819	2.050	2.124	2.283	2.448	2.720	2.241	16.6749
1200	1.967	2.016	2.151	2.340	2.473	2.633	2.263	11.3254
1400	1.917	2.046	2.182	2.299	2.443	2.678	2.261	12.3665

5 Conclusions

(1) The high-entropy pyrosilicates transform gradually from β-phase to γ-phase with an increase in the average radius of the RE^{3+} ion. When $\overline{r}(RE^{3+}) \leqslant$ 1.0588 Å, only the β-phase was formed in the high-entropy pyrosilicates. When 1.0647 Å $\leqslant \overline{r}(RE^{3+}) \leqslant$ 1.0688 Å, only the γ-phase was formed except in HE-6, and it comprised both β- and γ-phases with an average RE ionic radius of 1.0653 Å. When the average radius of the RE^{3+} ion exceeds a certain range ($\overline{r}(RE^{3+}) \geqslant$ 1.0810 Å), phases other than β-phase and γ-phase are generated.

(2) Both β-type and γ-type high-entropy pyrosilicates showed excellent phase stability with no phase transition of the temperature range from room temperature to 1400 ℃, which is the requirement for pyrosilicates to serve as EBC.

(3) The thermal expansion coefficient of β-type pyrosilicate is relatively constant, while the thermal expansion coefficient of γ-type pyrosilicate fluctuates within a certain range due to the difference in RE–O bond length and the high Δd of $[REO_6]^{9-}$ octahedron. β-type and γ-type pyrosilicate exhibit different anisotropic thermal expansion phenomena. Through composition design, the thermal expansion coefficient of γ-type high-entropy pyrosilicate can satisfy different types of CMCs.

Acknowledgements

This work was supported by the Instrument and Equipment Development, Chinese Academy of Sciences (YJKYYQ20210030) and Shanghai Science and Technology Innovation Action Plan (21142201100).

Declaration of competing interest

The authors have no competing interests to declare that are relevant to the content of this article.

Electronic Supplementary Material

Supplementary material is available in the online version of this article at https://doi.org/10.26599/JAC.2023.9220741.

References

[1] Chen ZL, Tian ZL, Zheng LY, *et al*. $(Ho_{0.25}Lu_{0.25}Yb_{0.25}Eu_{0.25})_2SiO_5$ high-entropy ceramic with low thermal conductivity, tunable thermal expansion coefficient, and excellent resistance to CMAS corrosion. *J Adv Ceram* 2022, **11**: 1279–1293.

[2] Raj R. Fundamental research in structural ceramics for service near 2000 ℃. *J Am Ceram Soc* 1993, **76**: 2147–2174.

[3] Padture NP. Advanced structural ceramics in aerospace propulsion. *Nat Mater* 2016, **15**: 804–809.

[4] Vaßen R, Kagawa Y, Subramanian R, *et al*. Testing and evaluation of thermal-barrier coatings. *MRS Bull* 2012, **37**: 911–916.

[5] Opila EJ. Oxidation and volatilization of silica formers in water vapor. *J Am Ceram Soc* 2003, **86**: 1238–1248.

[6] Dos Santos e Lucato SL, Sudre OH, Marshall DB. A method for assessing reactions of water vapor with materials in high-speed, high-temperature flow. *J Am Ceram Soc* 2011, **94**: S186–S195.

[7] Opila EJ. Variation of the oxidation rate of silicon carbide with water–vapor pressure. *J Am Ceram Soc* 1999, **82**: 625–636.

[8] Eaton HE, Linsey GD. Accelerated oxidation of SiC CMC's by water vapor and protection via environmental barrier coating approach. *J Eur Ceram Soc* 2002, **22**: 2741–2747.

[9] Liu PP, Zhong X, Niu YR, *et al*. Reaction behaviors and

mechanisms of tri-layer Yb_2SiO_5/$Yb_2Si_2O_7$/Si environmental barrier coatings with molten calcium–magnesium–alumino–silicate. *Corros Sci* 2022, **197**: 110069.
[10] Dong L, Liu MJ, Zhang XF, *et al*. Pressure infiltration of molten aluminum for densification of environmental barrier coatings. *J Adv Ceram* 2022, **11**: 145–157.
[11] Fernández-Carrión AJ, Allix M, Becerro AI. Thermal expansion of rare-earth pyrosilicates. *J Am Ceram Soc* 2013, **96**: 2298–2305.
[12] Zhong X, Niu YR, Zhu T, *et al*. Thermal shock resistance of Yb_2SiO_5/Si and $Yb_2Si_2O_7$/Si coatings deposited on C/SiC composites. *Solid State Phenom* 2018, **281**: 472–477.
[13] Sun LC, Luo YX, Ren XM, *et al*. A multicomponent γ-type $(Gd_{1/6}Tb_{1/6}Dy_{1/6}Tm_{1/6}Yb_{1/6}Lu_{1/6})_2Si_2O_7$ disilicate with outstanding thermal stability. *Mater Res Lett* 2020, **8**: 424–430.
[14] Felsche J. The crystal chemistry of the rare-earth silicates. In: *Structure and Bonding*. Cardin C, Duan X, Gade LH, *et al*. Eds. Berlin, Germany: Springer Berlin Heidelberg, 1973: 99–197.
[15] Turcer LR, Krause AR, Garces HF, *et al*. Environmental-barrier coating ceramics for resistance against attack by molten calcia–magnesia–aluminosilicate (CMAS) glass: Part II, β-$Yb_2Si_2O_7$ and β-$Sc_2Si_2O_7$. *J Eur Ceram Soc* 2018, **38**: 3914–3924
[16] Tian ZL, Ren XM, Lei YM, *et al*. Corrosion of $RE_2Si_2O_7$ (RE = Y, Yb, and Lu) environmental barrier coating materials by molten calcium–magnesium–alumino–silicate glass at high temperatures. *J Eur Ceram Soc* 2019, **39**: 4245–4254.
[17] Dong Y, Ren K, Lu YH, *et al*. High-entropy environmental barrier coating for the ceramic matrix composites. *J Eur Ceram Soc* 2019, **39**: 2574–2579.
[18] Dong Y, Ren K, Wang QK, *et al*. Interaction of multicomponent disilicate $(Yb_{0.2}Y_{0.2}Lu_{0.2}Sc_{0.2}Gd_{0.2})_2Si_2O_7$ with molten calcia–magnesia–aluminosilicate. *J Adv Ceram* 2022, **11**: 66–74.
[19] Xiang HM, Xing Y, Dai FZ, *et al*. High-entropy ceramics: Present status, challenges, and a look forward. *J Adv Ceram* 2021, **10**: 385–441.
[20] Wang X, Cheng MH, Xiao GZ, *et al*. Preparation and corrosion resistance of high-entropy disilicate $(Y_{0.25}Yb_{0.25}Er_{0.25}Sc_{0.25})_2Si_2O_7$ ceramics. *Corros Sci* 2021, **192**: 109786.
[21] Chen ZY, Lin CC, Zheng W, *et al*. Investigation on improving corrosion resistance of rare earth pyrosilicates by high-entropy design with RE-doping. *Corros Sci* 2022, **199**: 110217.
[22] Lee KN, Eldridge JI, Robinson RC. Residual stresses and their effects on the durability of environmental barrier coatings for SiC ceramics. *J Am Ceram Soc* 2005, **88**: 3483–3488.
[23] Fan CY, Zou BL, Zhu L, *et al*. Oxidation and thermal shock resistant properties of Si/Yb_2SiO_5/$NdMgAl_{11}O_{19}$ coating deposited on C_f/SiC composites. *Mater Design* 2017, **116**: 261–267.
[24] Lee KN, Fox DS, Bansal NP. Rare earth silicate environmental barrier coatings for SiC/SiC composites and Si_3N_4 ceramics. *J Eur Ceram Soc* 2005, **25**: 1705–1715.
[25] Shannon RD. Revised effective ionic radii and systematic studies of interatomic distances in halides and chalcogenides. *Acta Cryststallogr A* 1976, **32**: 751–767.
[26] Teng CY, Gauvin R. The *f*-ratio model for quantitative X-ray microanalysis. *Talanta* 2021, **235**: 122765.
[27] Chen H, Xiang HM, Dai FZ, *et al*. High entropy $(Yb_{0.25}Y_{0.25}Lu_{0.25}Er_{0.25})_2SiO_5$ with strong anisotropy in thermal expansion. *J Mater Sci Technol* 2020, **36**: 134–139.
[28] Newnham RE. *Properties of Materials: Anisotropy, Symmetry, Structure*. Oxford, UK: Oxford University Press, 2005.
[29] MacLaren I, Richter G. Structure and possible origins of stacking faults in gamma-yttrium disilicate. *Philos Mag* 2009, **89**: 169–181.
[30] Liu RH, Chen HY, Zhao KP, *et al*. Entropy as a gene-like performance indicator promoting thermoelectric materials. *Adv Mater* 2020, **29**: 1702712.
[31] Teng Z, Tan YQ, Zeng SF, *et al*. Preparation and phase evolution of high-entropy oxides $A_2B_2O_7$ with multiple elements at A and B sites. *J Eur Ceram Soc* 2021, **41**: 3614–3620.
[32] Cameron M, Sueno S, Prewitt CT, *et al*. High-temperature crystal chemistry of acmite, diopside, hedenbergite jadeite, spodumene and ureyite. *Am Mineral* 1973, **58**: 594–618.
[33] Brown G, Prewitt CT. High-temperature crystal chemistry of hortonolite. *Am Mineral* 1973, 58: 577–587.
[34] Smyth JR, High temperature crystal chemistry of fayalite. *Am Mineral* 1975, **60**: 1092–1097.
[35] Shankland TJ, Bass JD. *Elastic Properties and Equations of State*. Washington D.C., USA: American Geophysical Union, 1988.
[36] Wu J, Wei XZ, Padture NP, *et al*. Low-thermal-conductivity rare-earth zirconates for potential thermal-barrier-coating applications. *J Am Ceram Soc* 2002, **85**: 3031–3035.